

1 **Biomimetic curvature and tension-driven membrane**
2 **fusion induced by silica nanoparticles**

3

4 *Marcos Arribas Perez¹ and Paul A. Beales^{1,2,*}*

5

6 ¹ Astbury Centre for Structural Molecular Biology and School of Chemistry, University of Leeds,
7 Leeds, LS2 9JT, UK.

8 ² Bragg Centre for Materials Research, University of Leeds, Leeds, LS2 9JT, UK.

9

10 * Correspondence: p.a.beales@leeds.ac.uk

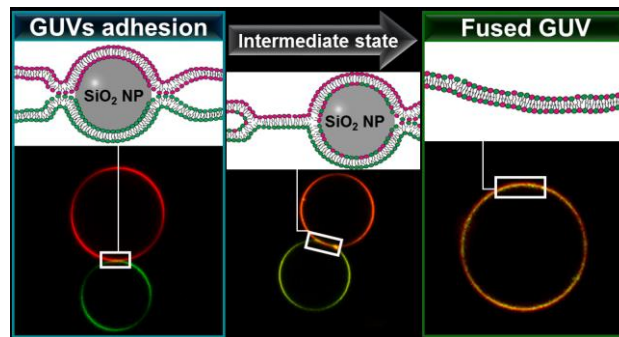
11

12

13 **Abstract**

14 Membrane fusion is a key process to develop new technologies in synthetic biology, where
15 artificial cells function as biomimetic chemical microreactors. Fusion events in living cells are
16 intricate phenomena that require the coordinate action of multicomponent protein complexes.
17 However, simpler synthetic tools to control membrane fusion in artificial cells are highly desirable.
18 Native membrane fusion machinery mediates fusion driving a delicate balance of membrane
19 curvature and tension between two closely apposed membranes. Here we show that silica
20 nanoparticles (SiO_2 NPs) at a size close to the cross-over between tension-driven and curvature-
21 driven interaction regimes initiate efficient fusion of biomimetic model membranes. Fusion
22 efficiency and mechanisms are studied by Förster Resonance Energy Transfer (FRET) and
23 confocal fluorescence microscopy. SiO_2 NPs induce a slight increase in lipid packing likely to
24 increase the lateral tension of the membrane. We observe a connection between membrane
25 tension and fusion efficiency. Finally, real-time confocal fluorescence microscopy reveals three
26 distinct mechanistic pathways for membrane fusion. SiO_2 NPs show significant potential for
27 inclusion in the synthetic biology toolkit for membrane remodelling and fusion in artificial cells.

28



29 **Keywords:** Artificial cells, membrane remodelling, bionanotechnology, lipid bilayers, lipid mixing,
30 membrane biophysics.

31

32

33 Membrane fusion is a key communication and transport process in living cells that is highly
34 desirable to replicate in artificial cell systems to control chemical compartmentalisation and trigger
35 targeted chemical processes. The life of cells is largely dependent on membrane fusion
36 processes. Eukaryotic cells require sequential fusion events to transport substances between
37 membrane-bound organelles, to release molecules to the extracellular environment or to
38 incorporate nutrients via endocytosis. ^{1,2}

39 Cell-sized giant unilamellar vesicles (GUVs) are common model architectures used in
40 synthetic biology as plasma membrane mimics. ^{3,4} Due to their ability to reproduce biological
41 processes, these minimal protocells are excellent platforms for the study of complex biological
42 processes (e.g. membrane fusion) in a simpler context. ^{5,6} Furthermore, these artificial systems
43 can encapsulate chemical reactions with potential biotechnological applications. ⁷⁻¹⁰ Therefore,
44 membrane fusion can be exploited to modify the composition of the membrane, the volume,
45 surface area and shape of the vesicle as well as to trigger chemical reactions and complex
46 metabolic cascades by delivering energy sources, enzymes, protein complexes or chemical
47 substrates into the lumen of the artificial cell. ¹¹⁻¹³

48 Mechanistic models for membrane fusion involve a series of sequential intermediate steps.
49 The process begins with the docking of two membranes. This is followed by the destabilisation of
50 the lipids by inducing these membranes to curve towards each other and increasing their local
51 lateral tension. This leads to the hemifusion of the contacting outer leaflets followed by the final
52 formation and expansion of a full fusion pore, which completes the process. ^{14,15} In living cells,
53 membrane fusion is regulated and catalysed by the coordinated action of protein complexes,
54 among which the SNARE proteins are possibly the best known. ² However, proteins are not
55 essential to trigger membrane fusion of lipid vesicles *in vitro*. Protein-free membrane fusion can
56 be achieved using other chemical stimuli, including particular membrane compositions, ^{16,17}
57 membrane-anchored DNA, ¹⁸ peptides ^{19,20} and multivalent ions ²¹ or by physical stimuli such as

58 optical tweezers,^{22, 23} electric pulses,²⁴ or local heating by gold nanoparticles.²⁵ All these fusion
59 strategies (including proteins) share the ability to induce one or more changes in membrane
60 tension, curvature, fluidity, or other biophysical properties of the membrane which can lower the
61 energy barrier to membrane fusion with varying degrees of efficiency.

62 Engineered nanoparticles (NPs) have the ability to interact with lipid membranes. The
63 strength of the NP-membrane interaction is determined by the physicochemical properties of the
64 NPs and the membrane as well as by the properties of the medium where the interaction occurs
65²⁶ and, depending on the strength of these interactions, the NPs cause multiple membrane
66 perturbations.²⁷ For instance, Contini *et al.* have reported that gold nanoparticles (AuNPs) with a
67 diameter equal or below 10 nm undergo cooperative adsorption and can form tubular
68 deformations in the membrane while the adsorption and the ability to bend membranes of larger
69 AuNPs is significantly reduced.²⁸ Another study has shown that gold nanoparticles and silica
70 nanoparticles weakly bound to the membrane can promote the adhesion of GUVs, while stronger
71 binding induces vesicle tubulation and destruction.²⁹ The ability of NPs to deform membranes
72 and facilitate remodelling processes can be exploited in synthetic biology to develop new tools to
73 efficiently trigger and control membrane fusion. An example of a NP-based fusion system has
74 been recently presented by Tahir *et al.* who designed amphiphilic nanoparticles composed of a
75 gold core functionalized with a mixed monolayer of alkanethiol ligands able to perform calcium-
76 triggered membrane fusion³⁰.

77 In this work, we introduce silica nanoparticles (SiO₂ NPs) as a potential tool to induce fusion
78 of biomimetic lipid membranes. SiO₂ NPs are able to interact with lipid membranes and induce
79 different membrane perturbations depending on their size and surface functionalisation.³¹⁻³³ A
80 previous work has shown a cross-over between high tension solidification and rupture of lipid
81 membranes by small SiO₂ NPs and wrapping of larger SiO₂ NPs by the membrane, where the
82 membrane adhesion and curvature elastic energies are calculated to equate for SiO₂ NPs with

83 diameters in the range of 28 – 40 nm.³¹ We hypothesise that SiO₂ NPs in this intermediate size
84 range will provide a balance between membrane curvature and membrane tension analogous to
85 the physical membrane perturbations induced by natural membrane fusion complexes. Hence,
86 we investigate the potential for 30 nm diameter SiO₂ NPs as artificial membrane fusion machinery.
87 The efficiency of these SiO₂ NPs in promoting lipid mixing, considered an essential consequence
88 of membrane fusion events, in populations of large unilamellar vesicles (LUVs) is studied using a
89 Förster Resonance Energy Transfer (FRET) assay. However, this method is insufficient to
90 investigate the mechanisms involved in fusion events. For this reason, we perform further
91 confocal microscopy studies of giant unilamellar vesicles (GUVs), which allows time-resolved
92 investigation of the trajectories of fusion events between individual pairs of GUVs. Direct imaging
93 of kinetic pathways of membrane fusion permits identification of intermediate fusion states and
94 quantification of the rate of lipid mixing between fusing GUVs in order to propose a mechanistic
95 interpretation of the process.

96

97 **RESULTS**

98 **SiO₂ NPs characterisation**

99 The SiO₂ NPs employed in this investigation are nanospheres of 30.8 ± 3.9 nm diameter as
100 characterised by Transmission Electron Microscopy (Figure S1). A similar size distribution is
101 observed using Dynamic Light Scattering (DLS) (Table S1). DLS measurements also show that
102 the SiO₂ NPs are colloidally stable in the experimental buffer (20 mM HEPES, 150 mM NaCl, at
103 pH 7.4) for at least 48 h (Figure S2), a time much longer than any of the experiments presented
104 below. Thus, these SiO₂ NPs have appropriate colloidal stability to investigate their application as
105 a trigger for membrane fusion. These SiO₂ NPs are negatively charged as indicated by their zeta

106 (ζ) potential (-18.2 ± 1.8 mV) determined using Dynamic Electrophoretic Light Scattering Analysis
107 (DELSA).

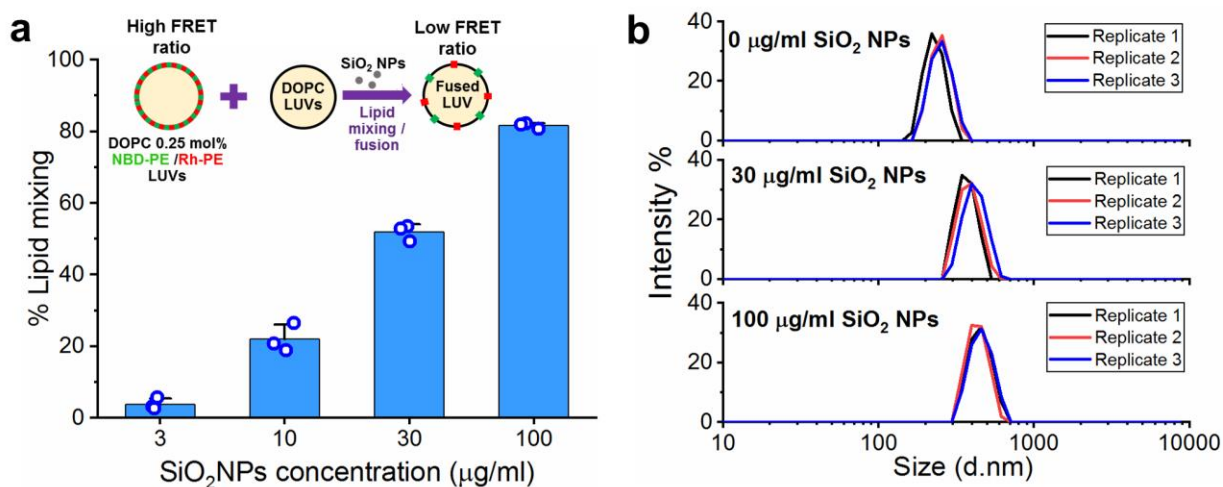
108 **SiO₂ NPs induce intervesicular lipid mixing**

109 The fusogenic activity of SiO₂ NPs is initially evaluated by a lipid mixing assay based on
110 FRET.³⁴ DOPC LUVs labelled with both NBD-DOPE and Rh-DOPE are mixed with probe-free
111 DOPC LUVs at a 1:5 ratio and exposed to different concentrations of SiO₂ NPs for 30 min. The
112 values for full lipid mixing are obtained from samples containing only LUVs labelled with 0.05
113 mol% NBD-DOPE and Rh-DOPE, which represent the maximum dilution of the probes in the
114 membrane that can be reached in our experiments.

115 The samples not treated with SiO₂ NPs show a maximum FRET ratio because both
116 fluorophores are closely colocalised in the labelled LUVs. However, the exposure to SiO₂ NPs
117 induce a decrease in FRET ratio, which is indicative of dose-dependent lipid mixing between
118 vesicles (Figure S3). Our results show that nearly 50% lipid mixing is reached when the LUVs are
119 incubated with 30 μ g/ml SiO₂ NPs and around 80% lipid mixing happens when LUVs are exposed
120 to 100 μ g/ml SiO₂ NPs (Figure 1a). The presence of SiO₂ NPs in solution promotes the exchange
121 of lipids between labelled and unlabelled LUVs, hence the distance between the donor and
122 acceptor fluorophores increases as they get diluted into the unlabelled membranes and the FRET
123 signal drops. However, these results must be interpreted carefully since the changes in FRET
124 signal are not exclusively produced by fusion but can result from other processes such as
125 hemifusion³⁵ and rupture of the vesicles.³⁶

126 The complete fusion of liposomes upon interaction with SiO₂ NPs would lead to a larger
127 population of vesicles. Hence, we used DLS to measure changes in the hydrodynamic size of
128 LUVs after exposure to SiO₂ NPs with the aim to assess whether SiO₂ NPs induce complete fusion
129 of LUVs. We observe that the size distribution of LUVs increases after incubation with 30 μ g/ml
130 and 100 μ g/ml SiO₂ NPs for 30 min from 347.40 ± 14.05 nm to 482.90 ± 52.02 nm and $564.10 \pm$

131 23.23 nm, respectively, thus a large proportion of the LUVs in the sample has fused into larger
 132 vesicles (Figure 1b, Table S1). Assuming that vesicle volumes are conserved during fusion
 133 events, these increases in vesicle size distributions are equivalent to, on average, 2.7 vesicles
 134 (30 $\mu\text{g}/\text{ml}$) and 4.3 vesicles (100 $\mu\text{g}/\text{ml}$) fusing with one another to form the larger vesicle
 135 population. These estimates are consistent with the 50% and 80% lipid mixing values reported by
 136 FRET at these NP concentrations when starting from an initial 1:4 mixture of labelled to unlabelled
 137 vesicles.



138

139 Figure 1. a) Percentage of lipid mixing induced by SiO₂ NPs obtained by FRET. Lipid mixing is detected as a
 140 decrease of FRET ratio in samples containing unlabelled DOPC LUVs and DOPC LUVs labelled with NBD-DOPE
 141 and rhodamine-DOPE (inset). The lipid mixing rises as the LUVs population is exposed to increased
 142 concentrations of SiO₂ NPs. b) Hydrodynamic size distribution of DOPC LUVs before (0 $\mu\text{g}/\text{ml}$ SiO₂ NPs) and
 143 after exposure to 30 $\mu\text{g}/\text{ml}$ and 100 $\mu\text{g}/\text{ml}$ SiO₂ NPs for 30 minutes measured by DLS. After incubation with SiO₂
 144 NPs the size of the LUVs increases.

145

146 SiO₂ NPs induce fusion of GUVs

147 Next, we used confocal microscopy to directly observe the ability of SiO₂ NPs to promote
 148 fusion of DOPC GUVs. Initially, we recorded the fate of GUVs labelled with 0.5 mol% Rh-DOPE
 149 (Rh-GUVs) after exposure to 25 $\mu\text{g}/\text{ml}$ SiO₂ NPs. Importantly, our observations clearly confirm the
 150 ability of SiO₂ NPs to trigger fusion of apposing GUVs, but not all the fusion events occur in the

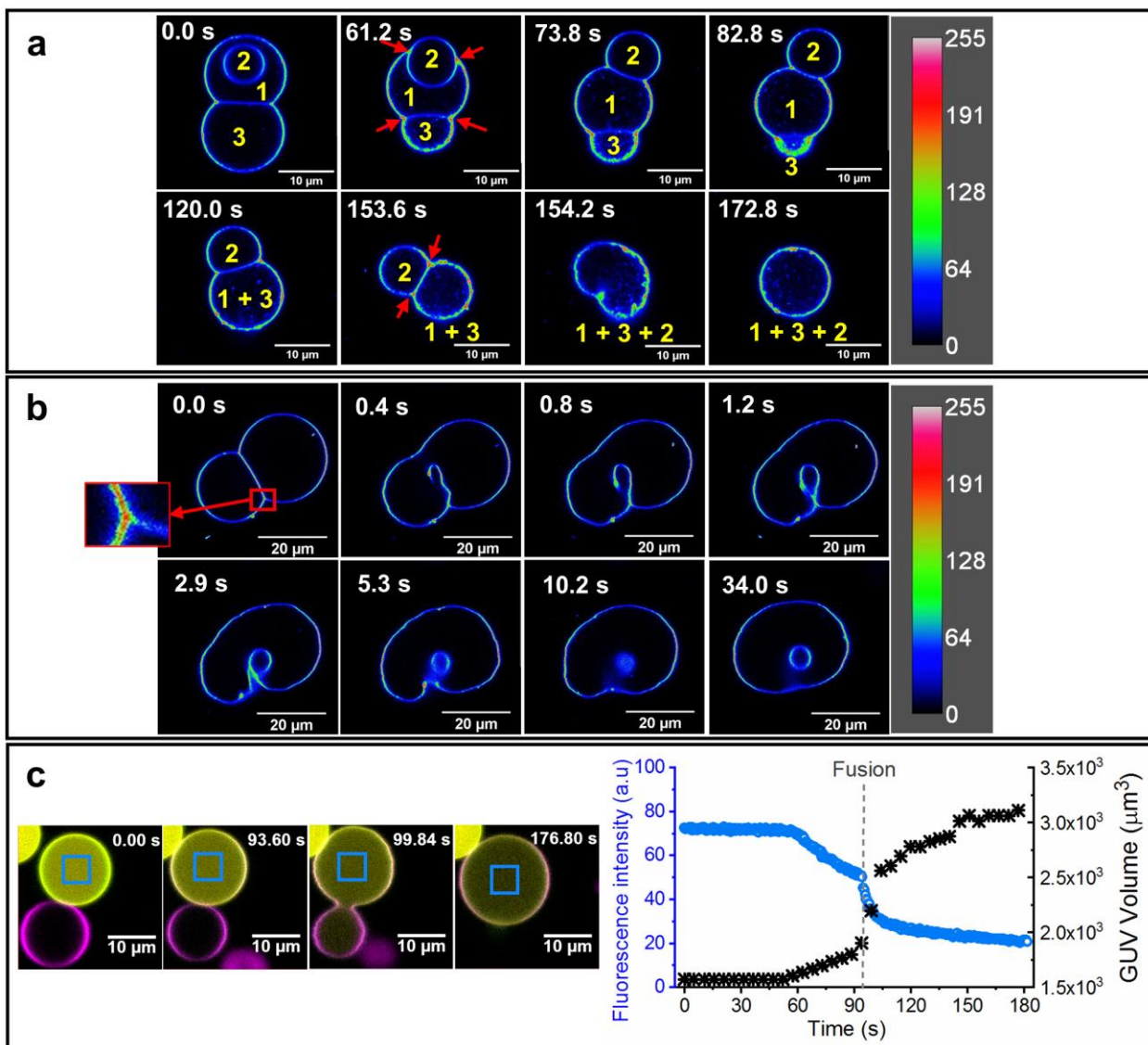
151 same manner. We observe that various processes, involving distinct morphological changes of
152 GUVs, can lead to membrane fusion (Figure 2a and 2b, Supplementary movies 1 and 2).

153 Figure 2a shows a sequence of two fusion processes occurring between two apposed
154 GUVs, one of them with a third GUV inside. Initially, one of the GUVs begins to shrink and its
155 membrane is apparently transferred to the neighbour GUV which progressively gets bigger. At
156 the same time, the third GUV, which was inside the growing one, is expelled from the lumen.
157 These two GUVs remain attached to each other and slowly get smaller until eventually their
158 membranes fuse resulting in a single final GUV (Supplementary Movie 1). A different mechanism
159 is observed in Figure 2b, where the fusion occurs after the sudden breakage of the membrane at
160 one end of the GUV contact region. The part of the membrane where the GUVs were in contact
161 gets trapped in the lumen of the new fused GUV and quickly rearranges to form an intraluminal
162 vesicle (Supplementary Movie 2).

163 In Figures 2a and 2b, we observe an increase of the fluorescence intensity at the vertices
164 of the membrane interface which separates the GUVs. This local rise in fluorescence intensity
165 likely denotes that three bilayers are contacting at these points, one bilayer from each GUV and
166 a mixed bilayer formed at the interface, commonly named as hemifusion diaphragm. In these
167 junctions, the membranes are under a high curvature stress and the lipids are condensed and
168 tightly packed showing enhanced fluorescence. The formation of intermediate fusion states and
169 other mechanistic aspects of the fusion process will be discussed in more detail later in the
170 manuscript.

171 In order to observe whether the contents of the DOPC GUVs mix upon vesicle fusion, we
172 carried out additional experiments mixing a population of GUVs encapsulating a sucrose solution
173 with a second GUV population containing a mixture of sucrose and fluorescence TRITC-dextran
174 (70 kDa). By analysing the fluorescence intensity of the GUV cargo during the fusion process we
175 observed that the fusion triggered by SiO_2 lead to a complete mix of the lumens of the GUVs

176 (Figure 2c, Supplementary movie 3). In Figure 2c, before the GUVs fully fuse, there is a lipid
 177 transfer between the GUVs which results in the simultaneous swelling of the fluorescently loaded
 178 vesicle and shrinking of the contiguous GUV. This swelling causes a gradual dilution of the TRITC
 179 in the lumen and explains the gradual drop of its fluorescent observed before the GUVs fully fuse.
 180 Once the GUVs fuse, the lumens of the two GUVs mix completely, consequently the fluorescent
 181 dextran molecules get diluted in the final lumen and the fluorescent intensity of the GUV cargo
 182 decreases steeply.



183

184 Figure 2. Confocal microscopy images of fusion processes of GUVs triggered upon exposure to 25 $\mu\text{g/ml}$ SiO_2
185 NPs. In panels a and b, GUVs are labelled with of Rh-DOPE and its fluorescence is presented as a pseudocolor
186 associated to the intensity as indicated in the colour code scale. a) Initially two GUVs are docked (1 and 3) and
187 the first one has a third vesicle inside (2). As time progresses, the GUV 3 gradually merges into the GUV 1 and at
188 the same time GUV 2 is ejected. The resulting 1+3 GUV and GUV 2 remain attached and the former start shrinking.
189 Eventually the GUVs fuse originating a single final GUV 1+3+2. b) The boundary membrane which separate the
190 two GUVs suddenly breaks at one end and the GUVs fuse. A membrane fragment gets trapped in the lumen of
191 the new GUV and spontaneously adopt a spherical configuration forming an intraluminal vesicle. Red arrows
192 indicate regions of increased fluorescence intensity observed at the edges of the docking regions. c) Micrographs
193 showing the lumen mixing process during fusion. One of the GUVs, labelled with 1 mol% DiO (green) is loaded
194 with a mixture of sucrose and TRITC-dextran 70 kDa (yellow) and the other is labelled with 1 mol% DiD (magenta)
195 and its lumen contains only sucrose (non-fluorescent). The plot shows the fluorescence intensity of TRITC-dextran
196 (blue circles, blue y-axis) in the region of the GUV lumen indicated by the blue box in the micrographs as well as
197 the volume of the GUV loaded with TRITC-dextran (black crosses, black y-axis) against time. The drop in
198 fluorescence intensity before fusion corresponds with the swelling of the GUV. After fusion, the lumens of the two
199 GUVs mix inducing a sharp drop of fluorescent intensity in the lumen of the resultant GUV.

200

201 **Influence of lipid packing and membrane tension on fusion processes**

202 In membrane fusion events, lipid packing defects are considered as an initial step required
203 for two adjacent membranes to fuse.^{30, 37, 38} Since previous studies on NP-membrane interactions
204 have shown that SiO_2 NPs produce perturbations in lipid packing and membrane fluidity,^{31, 33, 39}
205 we used Laurdan spectral imaging to quantify changes in lipid packing and membrane hydration
206 of DOPC GUVs labelled with 0.5 mol% Laurdan after incubation with 25 $\mu\text{g/ml}$ SiO_2 NPs.

207 Our results show that SiO_2 NPs induce a mild but statistically significant increase in the
208 average generalised polarisation (GP) of the Laurdan molecules embedded in the membrane
209 (Figure 3a). The increase in GP correspond to a less hydrated membrane with the lipids more
210 tightly packed. The adsorption of the SiO_2 NPs onto the GUVs is likely to create local highly curved
211 deformations in the membrane. In addition, the negative surface charge of SiO_2 NPs is likely to
212 alter the tilt angle of the DOPC headgroup dipole leading to a condensation of the lipids and a
213 reduction of the polarity of the membrane which increase the tension of the membrane and reduce
214 its polarity, facilitating the contact between closely localised membranes.^{16, 31, 40, 41} The high local
215 membrane curvature along with the increased membrane tension can lead to lipid packing defects
216 and unfavourable exposure of hydrophobic lipid tails to the aqueous environment. These packing

217 defects can be compensated in the contact zone between two membranes as the exposed lipid
218 tails of the inner monolayer of one membrane can match the exposed hydrophobic region of the
219 adjacent membrane.

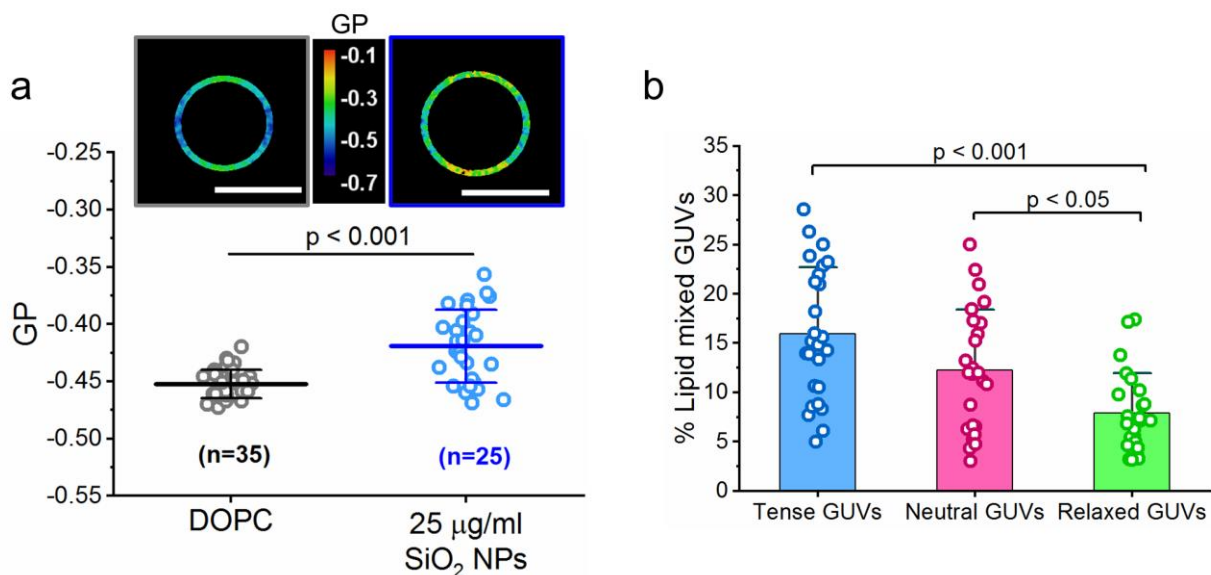
220 Next, we investigated the effect of the membrane tension in the fusion process. Membrane
221 tension is known to be a crucial biophysical parameter for the progress of membrane fusion
222 events.⁴¹⁻⁴⁵ Hence, we investigated the effect of the membrane tension in the fusion process
223 triggered by SiO₂ NPs.

224 The first step to assess the influence of membrane tension in the fusion process was to
225 modify the tension of the GUVs after electroformation by incubating them in hypertonic, isotonic
226 or hypotonic buffer overnight to obtain “relaxed”, “neutral”, or “tense” GUVs, respectively. Then,
227 to quantify the proportion of GUVs undergoing fusion in the sample we mixed equally tense Rh-
228 GUVs and DiO-GUVs (DOPC labelled with 1 mol% DiO) in a 1:1 volume ratio before adding the
229 SiO₂ NPs (25 µg/ml). Finally, after incubating the GUVs with the NPs for 30 min we took tile scans
230 and counted the proportion of GUVs with both dyes colocalised in the membrane (lipid mixed
231 GUVs).

232 The images of vesicles incubated in isotonic buffer show an average proportion of lipid
233 mixed and fused GUVs of 12.25 % from the total number of GUVs. The osmotic relaxation of the
234 GUVs reduces the mean proportion of lipid mixed GUVs in the samples to 7.90 %, while in the
235 samples of osmotically tensed GUVs the average percentage of vesicles fusing rises to 15.96 %
236 (Figure 3b). The tile scans were taken from 5 independent samples for each condition. These
237 data denote a clear impact of the membrane tension on the fusion process induced by the SiO₂
238 NPs. Similar results were obtained for LUVs measured by FRET spectroscopy (Figure S4). Note
239 that from the confocal microscopy images we are only counting the fusion events occurring
240 between oppositely labelled GUVs, but fusions between GUVs labelled with the same dye are
241 also taking place. In our samples, a Rh-GUV has the same probability to fuse with a DiO-GUV

242 than with another Rh-GUV, and the same applies for a DiO-GUV. Therefore, the proportion of
 243 GUVs undergoing fusion in our samples is, in theory, double than that quantified in the images.
 244 Also note that the proportion of fused GUVs is likely lower than that observed in LUV experiments
 245 due to the much larger GUVs exhibiting limited diffusion compared to LUVs, significantly reducing
 246 the number of collision events between these vesicles, which are required to facilitate membrane
 247 adhesion and fusion.

248



249

250 Figure 3. Effect of SiO₂ NPs on membrane order and impact of membrane tension on fusion efficiency of GUVs.
 251 a) Spectral imaging of DOPC GUVs labelled with Laurdan before and after incubation with 25 µg/ml SiO₂ NPs. GP
 252 images of a control GUV and a GUV after exposure to SiO₂ NPs. The graph shows that the distribution of average
 253 GP of the GUVs analysed increases slightly after incubation with 25 µg/ml SiO₂ NPs. Data are presented as mean
 254 ± standard deviation, circles indicate each individual measurement (number of individual datapoints indicated in
 255 the plot). b) Percentage of lipid mixed GUVs observed in confocal microscopy images depending on the membrane
 256 tension after incubation with 25 µg/ml SiO₂ NPs. The plot indicates a clear relationship between membrane tension
 257 and the proportion of GUVs undergoing fusion. The bars show the mean and the error bars the standard deviation.
 258 The overlaid circles represent the proportion of lipid mixed GUVs in each image analysed (Tense GUVs = 26
 259 images; Neutral GUVs = 25 images; Relaxed GUVs = 24 images). The statistical significance in a and b was tested
 260 using a one-way ANOVA with a post-hoc Bonferroni test.

261

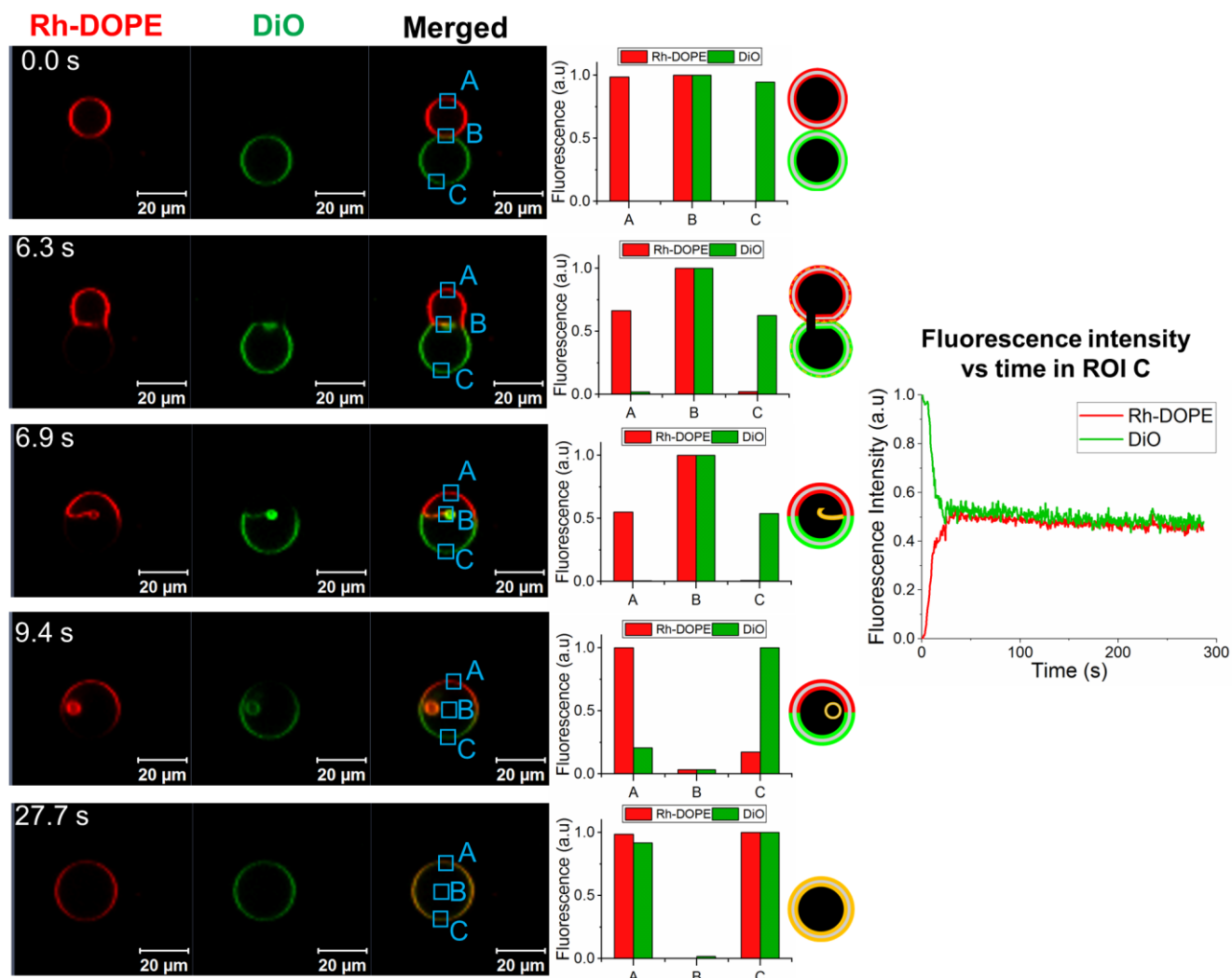
262 **Silica nanoparticles induce fusion of GUVs via three different pathways**

263 With the aim of getting a further mechanistic insight into the processes leading to membrane
264 fusion, we perform additional real-time confocal microscopy experiments to record single fusion
265 events between Rh-GUVs and DiO-GUVs. These experiments provide information about
266 intermediate states as well as the kinetics of the fusion process by detecting the lipid mixing
267 between GUV pairs.

268 First, we localise GUV pairs composed by one Rh-GUV and a DiO-GUV which show only
269 red and green fluorescence, respectively. After SiO₂ NPs are added to the sample, we monitor
270 changes in fluorescence intensity in each channel over time at the interface between vesicles and
271 the more distal regions of each GUV. Our observations show that once SiO₂ NPs interact with a
272 pair of GUVs, the vesicles adopt different intermediate states characterised by the degree of lipid
273 mixing before their eventual fusion. The fusion process begins with a localised merging of the
274 outer leaflets of the apposed GUVs as a result of high local curvature and lipid packing defects
275 induced by the SiO₂ NPs. From this point, depending on the different intermediate states and
276 morphological transitions that GUVs experience during a fusion event, we identify three main
277 fusion pathways triggered by SiO₂ NPs.

278 **Direct Full Fusion.** In the first pathway, no or marginal intervesicular lipid exchange is
279 observed before the GUVs fuse. The membrane breaks at one edge of the interface and the
280 GUVs suddenly fuse. Immediately following fusion to form a new GUV, the lipids from the original
281 vesicles are observed to be not yet mixed, showing two easily distinguishable hemispheres, one
282 green and one red, which then mix rapidly in the new merged membrane (Figure 4,
283 Supplementary Movie 4). The interaction of SiO₂ NPs with the membrane of the GUVs would
284 induce membrane defects which generate a large elastic stress at the rim of the docking region.
285 Such elastic stress is relaxed by the formation of a large pore which leads to full GUV fusion. The
286 membrane fragment formerly situated at the contact zone is trapped inside the new GUV and

287 reorganises quickly to form an intraluminal vesicle (Figures 4 and 2b). The analysis of the size
 288 of the final GUVs compared to the initial GUVs shows that the volume of the final GUV is
 289 equivalent to the sum of the volume of the two initial GUVs (Figure S5).



290
 291 Figure 4. Fusion of GUVs via the sudden full fusion pathway. Confocal microscopy images show the state of the
 292 GUVs at particular stages of the process. DOPC GUVs are labelled with Rh-DOPE (red channel) and DiO (green
 293 channel). The bar plots show the fluorescence intensity of each fluorophore measured at the ROIs indicated by
 294 the blue boxes. Cartoons are schematic representations of the lipid mixing and topological transformations
 295 occurring in at that particular time point. The bar plots indicate that lipid mixing occurs after the GUVs fuse. The
 296 membrane boundary gets trapped in the final GUV and reorganise originating an intraluminal vesicle. The line plot
 297 displays the evolution of the fluorescence intensity in both channels over time at the ROI C.

298

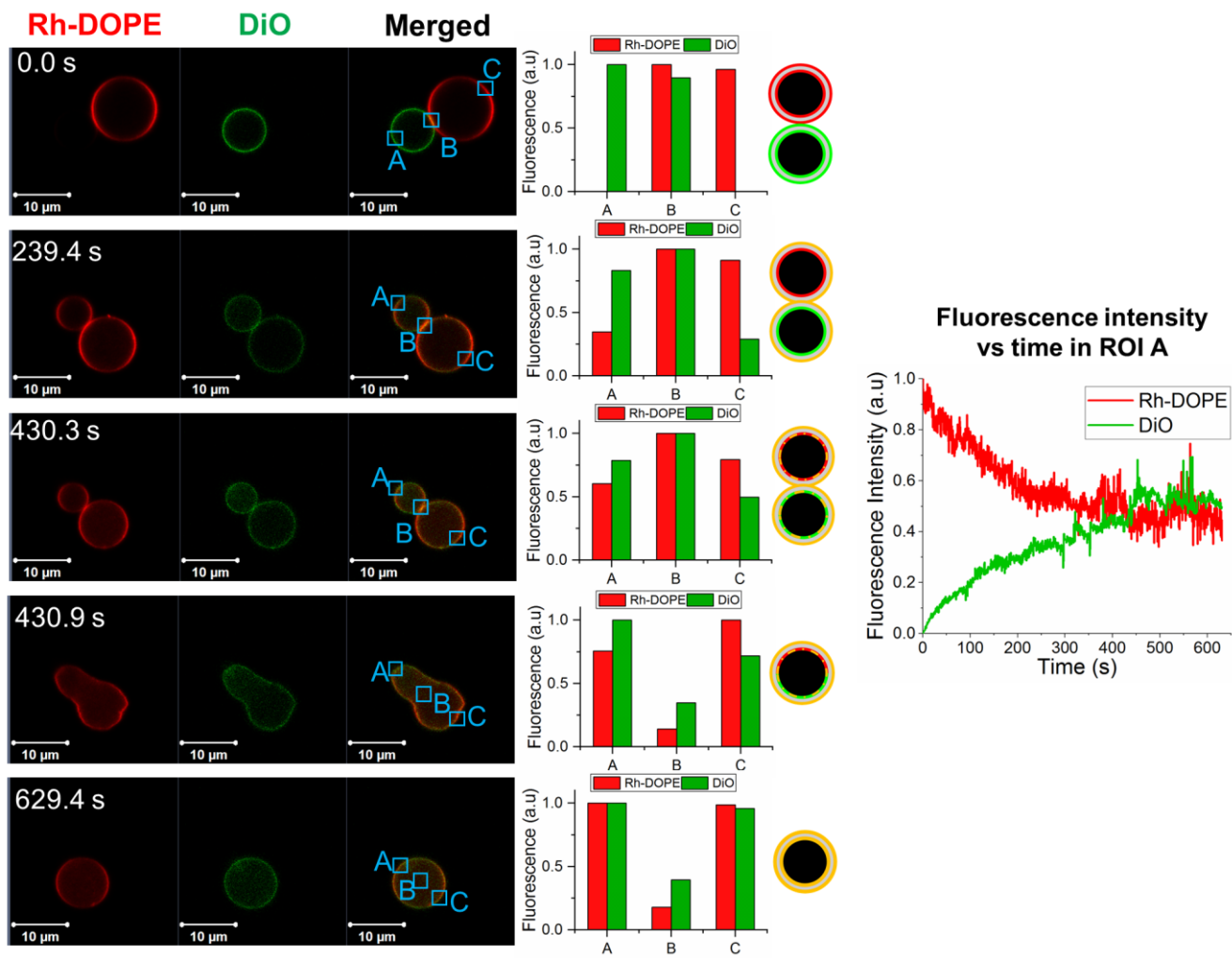
299

300 **Hemifusion – fusion.** In this pathway, a gradual bidirectional exchange of lipids between
301 the contacting GUVs is detected before the eventual fusion of the vesicles (Figure 5,
302 Supplementary Movie 5). This second fusion pathway resembles the classic fusion model in which
303 a hemifusion diaphragm intermediate precedes the formation of the fusion pore ^{40, 46}. A
304 hemifusion diaphragm is an intermediate state where the outer monolayers of the fusing GUVs
305 are merged and the inner monolayers form a mixed bilayer at the contact region.

306 The hemifusion intermediate is detected by the presence of both dyes in the same GUV. ¹⁶,
307 ⁴⁷ However, as only the lipids in the outer monolayer are mixed, the fluorescence intensity of the
308 “intruder dye” will be lower in this GUV than in the neighbour one where it is present in both
309 membrane leaflets. The lipids of the outer leaflets mix completely before the GUVs fuse, as
310 observed in Figure 5 (frame t=239.4 s). The enhanced fluorescence intensity displayed by both
311 dyes at the GUV interface is probably due to lipid condensation at the rim of the hemifusion
312 diaphragm. Images at longer times indicate a further level of lipid mixing, suggesting some extent
313 of interleaflet lipid exchange. Eventually, a fusion pore opens and expands quickly through the
314 hemifusion diaphragm and the GUVs fuse completing a classic hemifusion-fusion pathway. The
315 newly formed GUV progressively adopts the spherical shape typical of vesicles and the lipids get
316 homogeneously distributed across the membrane.

317 The analysis of the GUVs size before and after fusion reveals a volume loss while the GUVs
318 are hemifused (Figure S5). While the hemifusion is taking place, the GUVs slowly shrink and
319 bright dots appear in their lumen, suggesting that small vesicles or lipid aggregates are being
320 removed from the membrane by the SiO₂ NPs (Figure 5, Supplementary Movie 5). This loss of
321 membrane surface area is likely to increase the membrane tension and generate the elastic stress
322 needed for the opening of a fusion pore in the hemifusion diaphragm.

323



324

325 Figure 5. Fusion of GUVs via hemifusion-fusion pathway. Confocal microscopy images showing intermediate
 326 states of the fusion process. DOPC GUVs are labelled with Rh-DOPE (red channel) and DiO (green channel). The
 327 bar plots show the fluorescence intensity of each fluorophore measured at the ROIs indicated by the blue boxes.
 328 Cartoons are schematic interpretations of the data. The lipid mixing observed before the GUVs fuse indicates that
 329 a hemifusion intermediate has formed. Eventually the GUVs fuse. The fluorescence intensity observed in the lumen
 330 of the GUVs is likely to proceed from small patches of the membrane removed by the SiO₂ NPs. The line plot
 331 displays the evolution of the fluorescence intensity in both channels over time at the ROI A.

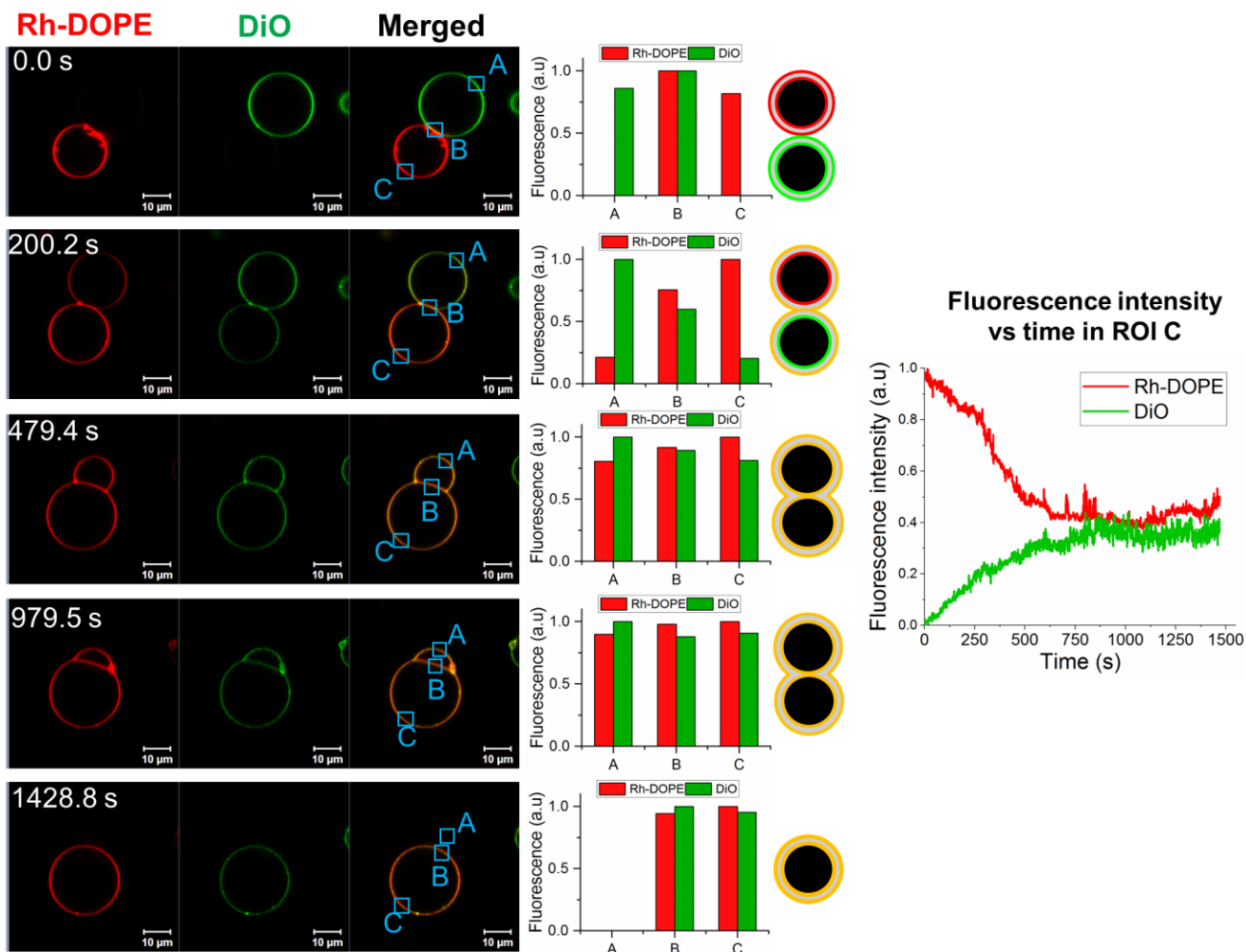
332

333

334

335 **Gentle merging.** Nevertheless, the fusion process cannot always be completed by the
336 opening of a fusion pore at the hemifusion diaphragm. In these occasions, one of the GUVs is
337 gradually absorbed by the other and their membranes fuse by a process that we have called
338 gentle membrane merging (Figure 6, Supplementary Movie 6). Like in the previous pathway, the
339 fluorescence intensity analysis indicates an initial lipid mixing just in the outer monolayers followed
340 by further lipid mixing in the inner monolayers. However, unlike the hemifusion-fusion pathway,
341 during these events there is a complete lipid mixing in both monolayers while the two GUVs are
342 still separated. We hypothesise that the elastic stress at which the membranes are subjected
343 would not be high enough to drive the opening of a large fusion pore at the hemifusion diaphragm.
344 Instead, the GUVs remain hemifused and one of them slowly shrinks and blends into the other
345 which grows accordingly. The result from these events is then a GUV formed by a mixture of the
346 membranes from the two initial GUVs and whose volume equals the sum of the volumes of the
347 initial vesicles (Figure S5).

348 We hypothesise an explanation to this phenomenon based on Laplace's law. Due to
349 differential pressure inside the GUVs and the formation of transient nanopores at the hemifusion
350 diaphragm, the GUV at higher Laplace pressure is "sucked" into the apposed GUV. Given that
351 the Laplace pressure (P) depends on the membrane tension (σ) and the radius of the vesicle (r)
352 as $\Delta P=2\sigma/r$, if the two GUVs have the same membrane tension, the smaller GUV would be
353 absorbed by the larger one. However, in our experiments, this is not always the case: sometimes
354 the larger GUV is engulfed by the smaller one. Therefore, in order for the pressure in the larger
355 GUV to be higher, its membrane must be significantly tenser than the membrane of the smaller
356 neighbouring vesicle. Hence the pressure differential would drive a flow from the larger and tenser
357 GUV to the smaller and more relaxed GUV.



358

359 Figure 6. Fusion of GUVs via gentle merging pathway. Confocal microscopy images show the state of the GUVs
 360 at different stages of the process. The DOPC GUVs are labelled with Rh-DOPE (red channel) and DiO (green
 361 channel). The bar plots show the fluorescence intensity of each fluorophore measured at the ROIs indicated by
 362 the blue boxes. Cartoons are schematic interpretations of lipid mixing membrane configuration state at the stage
 363 of the process shown in the micrographs. The lipid mixing observed before the GUVs fuse indicates that a
 364 hemifusion intermediate has formed. One of the GUVs gradually shrinks and the other GUV grows consequently.
 365 At the same time their membranes merge gently until forming a single GUV with a mixed membrane. The line plot
 366 displays the evolution of the fluorescence intensity in both channels over time at the ROI C.

367

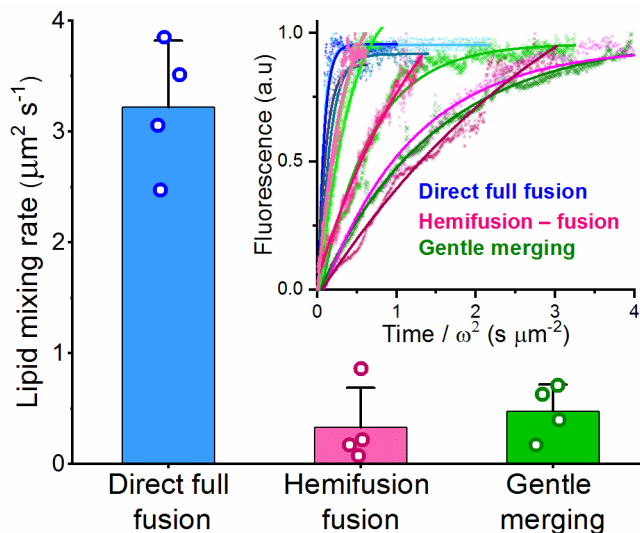
368

369 **The rate of lipid mixing is slower in fusion pathways involving hemifusion**
370 **intermediates**

371 Further analysis of the confocal time series allows quantification of the rate of lipid mixing
372 in the different fusion pathways. For this analysis, we measure the increase in fluorescence
373 intensity over time from the moment when one of the dyes begins to migrate into its neighbouring
374 vesicle.

375 The results summarised in Figure 7 show a much slower lipid mixing rate when the fusion
376 pathway involves the formation of a hemifusion diaphragm. The lipid mixing rate calculated from
377 the direct full fusion events ($3.22 \pm 0.60 \mu\text{m}^2 \text{s}^{-1}$) is consistent with literature values for the lateral
378 diffusion coefficient of DOPC^{31,48}, therefore in this pathway the lipid mixing is driven solely by the
379 lateral diffusion of lipids once the vesicles have fused.

380 In contrast, the lipid mixing rates estimated for the other two fusion pathways are
381 considerably slower than DOPC lateral diffusion, with values of $0.33 \pm 0.36 \mu\text{m}^2 \text{s}^{-1}$ for the
382 hemifusion-fusion pathway and $0.48 \pm 0.24 \mu\text{m}^2 \text{s}^{-1}$ for the gentle merging. Similar slow diffusion
383 of lipids has been reported previously in protein-free and SNARE-mediated hemifused GUVs.^{19,}
384⁴⁷ We observe that full bilayer mixing can be reached while the GUVs are hemifused. This bilayer
385 mixing results from enhanced lipid flip-flop between the membrane leaflets which considerably
386 reduces the rate of lipid mixing compared to lateral diffusion alone. Another potential contribution
387 to bilayer lipid mixing involves the formation of transient nanoscopic pores in the membrane which
388 allows short-lifetime pulses of lipid transfer between monolayers.



389

390 Figure 7. Rate of lipid mixing during each fusion pathway. The calculated average lipid mixing rate for the fusion
 391 events via direct full fusion is $3.22 \pm 0.60 \mu\text{m}^2 \text{s}^{-1}$ whereas the hemifusion-fusion pathway and the gentle merging
 392 show reduced lipid mixing rates, $0.33 \pm 0.36 \mu\text{m}^2 \text{s}^{-1}$ and $0.48 \pm 0.24 \mu\text{m}^2 \text{s}^{-1}$, respectively (The bar plot show the
 393 mean and standard deviation with the individual datapoints overlaid). The inset plot shows the normalised
 394 fluorescence intensity of the dye when it begins to colonise a membrane where it was not present initially as a
 395 function of time per unit area. The curves of individual events were fitted using an exponential function (see
 396 methods) to estimate the rate of lipid diffusion.

397

398 DISCUSSION

399 In this work, we introduce a novel, protein-free membrane fusion platform based on the
 400 ability of 30 nm SiO_2 NPs to trigger membrane curvature and tension that mimics the
 401 physicochemical effects of natural protein complexes for membrane fusion. Initial FRET
 402 experiments performed in bulk LUV populations show a significant increase in intervesicular lipid
 403 mixing dependent on the concentration of SiO_2 NPs in solution. The fusogenic activity of SiO_2
 404 NPs is confirmed by direct imaging of GUVs using confocal microscopy.

405 Figure 8 summarises our proposed nanoscale molecular mechanisms that occur as SiO_2
 406 NPs induce the contact and fusion of two membranes. Based on our observations, we propose a
 407 scenario where membrane tension is the principal driving force of the fusion events. This view
 408 agrees with many studies, including theoretical models,^{40, 49} simulations^{42, 43, 50} and experimental

409 investigations.^{44,51} In our system, the fusion process starts when SiO₂ NPs in suspension interact
410 with closely localised GUVs. This interaction is likely to favour the close approach between the
411 membranes of two GUVs by inducing local changes in membrane curvature. Molecular
412 simulations have shown that any protein complex located between two opposing membranes
413 generates a local membrane curvature that promotes the close apposition of the opposing leaflets
414 needed to begin the fusion process.⁵² In addition, we have seen that the SiO₂ NPs affect the lipid
415 packing within the membrane. The negative surface charge of SiO₂ NPs is predicted to produce
416 a reorientation of the headgroup dipole of DOPC lipids generating an electrostatic condensation
417 of the area per lipid in the outer membrane leaflet, which would generate a considerable increase
418 in membrane tension.⁵³

419 The increase in membrane tension generates elastic stress which, along with high local
420 membrane curvature and lipid packing defects, would result in highly energetically unfavourable
421 exposure of hydrophobic membrane regions to the aqueous environment. The elastic stress is
422 likely released by the reorganisation of the membranes in the boundary between the GUVs so the
423 exposed hydrophobic region of one membrane matches the hydrophobic region of the inner leaflet
424 of the adjacent membrane.¹⁶ The resulting structure would be a membrane stalk where the inner
425 monolayers of the neighbouring membranes form a bilayer in a small region where the GUVs are
426 docked. The outer leaflets of the vesicle membranes thus reorganise themselves into a highly
427 bent monolayer, which would be expected to begin to merge.⁵⁴ After the stalk is formed, GUVs
428 can follow three different observed pathways that lead to membrane fusion: i) direct full fusion, ii)
429 hemifusion-fusion and iii) gentle merging.

430 i). **Direct full fusion:** a significant increase in membrane tension would lead to full fusion
431 immediately after the stalk formation. The stalk presumably originates at the edge of the
432 boundary region but the persistent elastic stress would conceivably compel the membrane
433 to break, forming a pore which would be anticipated to expand laterally along the perimeter

434 of the docking zone. Consequently, the membrane region that was separating the individual
435 GUVs would get trapped inside the new GUV and therefore reorganise to avoid exposure
436 of hydrophobic lipid tails, forming an intraluminal vesicle. Analysis of lipid mixing rates
437 shows that once the GUVs have fused, lipids mix in the new bilayer via lateral diffusion.

438 A similar fusion mechanism was reported by Tanaka *et al.*, who observed that trivalent
439 lanthanum ions (La^{3+}) induce the fusion of DOPC GUVs.⁵⁵ They propose that the outer
440 monolayer of the membranes merge at one edge of the region where membranes are in
441 contact and this destabilises the packing of the lipid tails that causes the breakage of the
442 membrane leading to fused GUVs with an intraluminal vesicle. Moreover, previous studies
443 on vacuole fusion mediated by the SNARE complex have proposed that the formation of an
444 intraluminal vesicle during the fusion occurs when the fusion pore forms at one point on
445 the rim of the stalk and expands laterally along the perimeter entrapping a membrane
446 fragment, which becomes an intraluminal vesicle.^{56, 57} In one of these studies, Mattie and
447 colleagues showed that the expansion of the stalk into a hemifusion diaphragm inversely
448 correlates with intraluminal fragment formation.⁵⁷

449 ii). **Hemifusion-fusion pathway:** we propose that if the membrane tension is moderate, then
450 the elastic stress can be released by the stalk formation and its expansion into a hemifusion
451 diaphragm. The hemifusion diaphragm remains stable for a relatively long time in which the
452 lipids of the outer leaflets are observed to fully mix. The lipid mixing rate during hemifusion
453 is much slower than lateral diffusion. This slower lipid mixing can be explained by a slower
454 lipid flip-flop within the hemifusion diaphragm. We observe higher levels of lipid mixing
455 between GUVs, which must involve transfer of lipids between the inner membrane leaflets.
456 The formation of a stable hemifusion diaphragm implies that the surface area of the inner
457 leaflets of the membranes must be larger than that of outer monolayers. This requires the
458 transport of lipids from the outer leaflet to the inner monolayer via flip-flop. The lipid flip-flop

459 would be expected to be particularly enhanced at the rim of the hemifusion diaphragm. In
460 this region, the significant negative curvature of the membrane likely generates a
461 mechanical stress different in each monolayer and the membranes becomes highly
462 unstable. The differential mechanical stress derived from increased membrane curvature
463 as well as local membrane deformations are known to significantly increase the rate of
464 interleaflet lipid transport.^{58,59} Moreover, molecular dynamics simulations have shown that
465 lipid flip-flop is a preferential mechanism to reduce the instability at the junction site of three
466 bilayers and maintain a metastable hemifusion diaphragm.⁶⁰

467 Local membrane perturbations induced by the SiO₂ NPs and transient nanopores also
468 favour interleaflet lipid transfer. Such interleaflet lipid exchange would relax the stress in the
469 membrane by removing lipids from the compressed outer monolayer and adding them to
470 the expanded regions of the inner leaflets. However, this unidirectional lipid exchange could
471 generate an area mismatch between monolayers. Hence, to prevent this from happening,
472 lipids from the inner leaflet must also be transported to the outer monolayer.

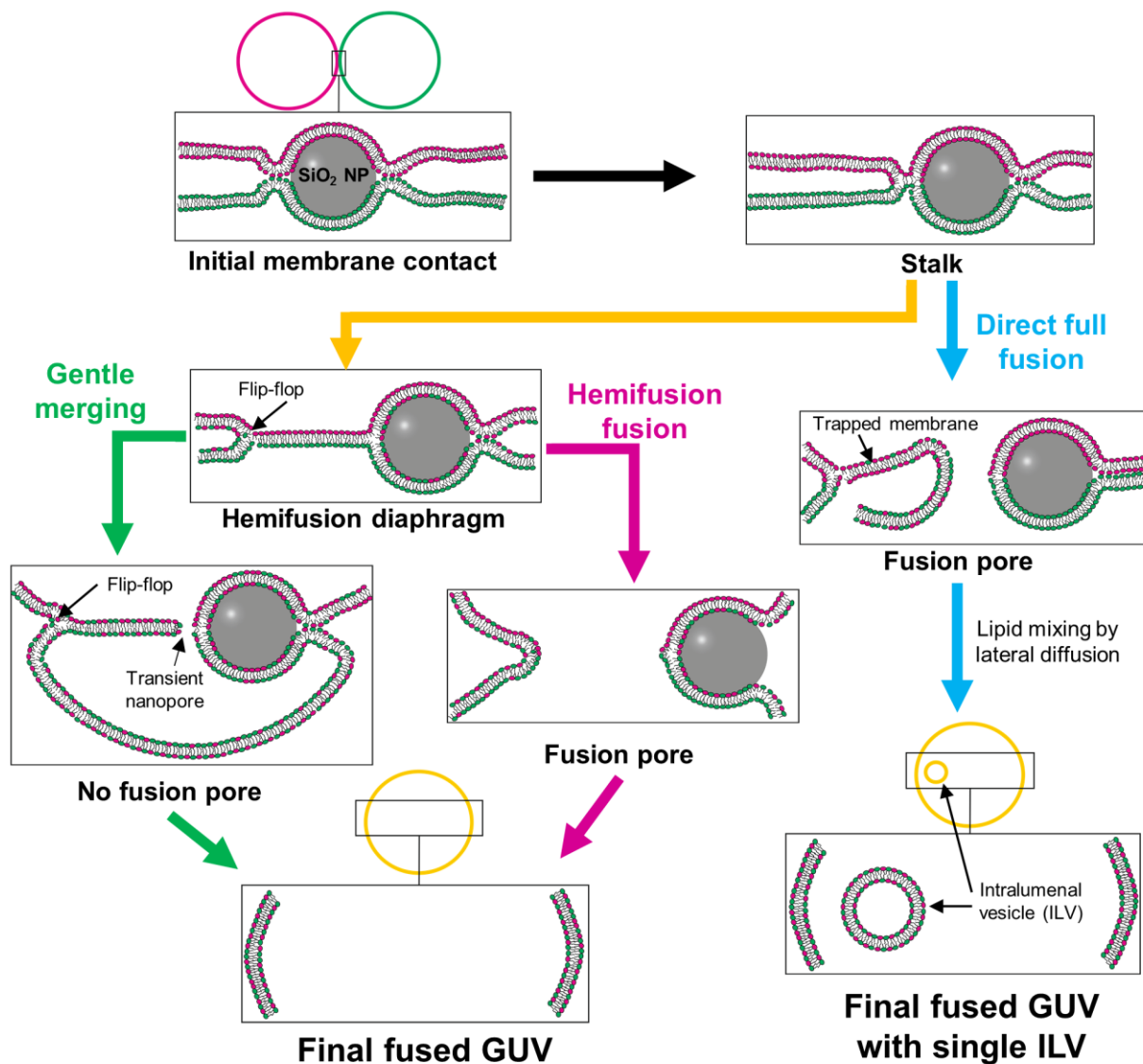
473 Before complete bilayer lipid mixing is achieved, a pore opens and expands through the
474 hemifusion diaphragm, finishing the fusion process. Strobl *et al* showed that SiO₂ NPs are
475 able to cross DOPC membranes and, during the process, they take small membrane
476 sections with them, inducing the shrinkage of the GUV and a rise in its membrane tension.

477 ⁶¹ This is very similar to what we observe in our experiments, hence the opening of the
478 fusion pore would seemingly be driven by a further increase in membrane tension induced
479 by SiO₂ NPs removing membrane surface area from the GUVs. In this case, the final GUV
480 does not show the single intraluminal vesicle characteristic from the direct full fusion
481 pathway.

482 iii). **Gentle membrane merging:** Although this pathway results in a single GUV formed by a
483 mixed membrane from the original vesicles, this process is different from the previous

484 pathway, and from other fusion events reported in the literature, because the fusion pore
485 does not expand across the hemifusion diaphragm, instead their membranes merge
486 gradually. During this process, the tension at the hemifusion diaphragm is presumably
487 stably maintained and the elastic stress could be totally relaxed at the rim of the hemifusion
488 diaphragm by enhanced flip-flop rate and potentially by the formation of transient nanosized
489 pores. As the lipid bilayers mix, one of the apposed GUVs gets progressively smaller and
490 its membrane is transferred to the neighbour vesicle which grows consequently, until the
491 shrinking GUV is completely engulfed and only one GUV with a fully mix membrane
492 survives. We propose that this phenomenon is promoted by differential membrane tension
493 between the docked GUVs. Transient pores must also occur in the shrinking vesicle to
494 facilitate its reduction in total volume. A different tension in each GUV would, according to
495 Laplace's law, generate a difference between their internal pressures, which will
496 presumably favour the tensor GUV gently merging into the less tense vesicle of the pair.

497 The fusogenic activity of SiO₂ NPs relies on its capacity to generate increased membrane
498 tension, high enough to overcome the different energy barriers during the fusion process. The
499 fastest but more energetically demanding process is the direct full fusion. Such high energetic
500 cost implies that the membrane tension acquired is not always sufficient to trigger this pathway.
501 However instead of aborting the process, the system finds an alternative route, the hemifusion
502 intermediate, which is slower but requires less energy. Similarly, if the energy needed for the
503 opening and expansion of a fusion pore cannot be overcome, the process is finished via gentle
504 membrane merging. Unfortunately, our experimental approach does not allow to quantify the
505 proportions of fusion events taking place through each different pathway, so different strategies
506 might be considered in the future to overcome this limitation and get more information about
507 biophysical parameters influencing which fusion pathway is going to be followed.



508

509 Figure 8. Schematic representation of membrane transitions occurring at the docking region during fusion events
 510 triggered by SiO₂ NPs. The SiO₂ NPs facilitate the initial contact between two membranes and induce high local
 511 curvature, increased tension and lipid packing defects. This promotes the formation of a stalk. At this point, a fusion
 512 pore can form directly from the stalk leading to a sudden full fusion of the GUVs. After the GUVs fuse the lipids in
 513 the membrane mix via lateral diffusion and the membrane previously placed at the boundary is trapped in the
 514 lumen and forms an intraluminal vesicle (Sudden full fusion pathway). The stalk can also expand into a hemifusion
 515 diaphragm stabilised by enhanced lipid flip-flop at its rim. If a fusion pore opens at the hemifusion diaphragm the
 516 fusion process is completed (Hemifusion-fusion pathway). However, if this does not happen the hemifusion
 517 diaphragm persists stabilised by flip-flop and transient nanopores. In this case, one of the GUVs is gradually
 518 absorbed by the other one and their membranes gently merge (Gentle membrane merging pathway).

519

520

521 Our results offer the prospect of using SiO₂ NPs as a new nanotechnological tool in synthetic
522 biology to create more complex model membrane systems, which better mimic the properties of
523 cell membranes. These systems would mix the cargo of two vesicles and trigger chemical
524 reactions. These NPs are inexpensive to produce, can remain colloidally stable in solution for long
525 periods of time and can easily be tuned to boost particular advantageous properties.

526 A current major challenge in the study of membrane remodelling processes is
527 understanding the role that Gaussian curvature plays in them. The experimental investigation of
528 Gaussian curvature is very challenging and requires membrane systems whose topology can be
529 tightly controlled.⁵² The fact that the same fusogen can induce membrane fusion *via* different
530 pathways represents an advantage for the study of membrane fusion mechanisms because it
531 implies that by changing particular conditions (membrane composition, vesicle shape, ionic
532 strength of the medium, presence of macromolecules and divalent cations such as Ca²⁺, etc.) the
533 system could be tuned to favour a specific fusion pathway over the others and give information
534 about the influence of specific parameters, such as membrane curvature and tension, in the fusion
535 process. Also, the surface of the SiO₂ NPs can be functionalised to increase or decrease their
536 affinity for the membrane. Therefore, SiO₂ NPs are a promising synthetic biology tool for triggering
537 membrane fusion in a broad range of experimental scenarios.

538

539 **METHODS**

540 **Materials**

541 DOPC (1,2-dioleoyl-sn-glycero-3-phosphocholine), Rh-DOPE (1,2-dioleoyl-sn-glycero-3-
542 phosphoethanolamine-N-(lissamine rhodamine B sulfonyl) (ammonium salt)), and NBD-DOPE
543 (1,2-dioleoyl-sn-glycero-3-phosphoethanolamine-N-(7-nitro-2-1, 3-benzoxadiazol-4-yl)
544 (ammonium salt)) were purchased from Avanti Polar Lipids Inc. (Alabaster, Alabama, USA).

545 Colloidal SiO₂ NPs LUDOX TM-50 (50 wt. % suspension in H₂O), Tetramethylrhodamine
546 isothiocyanate (TRICT)-Dextran 70 kDa, indium tin oxide (ITO) coated glass slides (surface
547 resistivity 8–12 V sq⁻¹), HEPES (4-(2-hydroxyethyl)-1-piperazineethanesulfonic acid), sodium
548 chloride (NaCl), sucrose (C₁₂H₂₂O₁₁), and bovine serum albumin (BSA) were obtained from
549 Sigma-Aldrich Co. (Gillingham, UK). DiO (3,3'-Diocetadecyloxycarbocyanine Perchlorate) and DiD
550 (1,1'-Diocetadecyl-3,3,3',3'-Tetramethylindodicarbocyanine, 4-Chlorobenzenesulfonate Salt) were
551 purchased from ThermoFisher Scientific Ltd. (Loughborough, Leicestershire, UK). Microscope μ-
552 slide 8 well glass bottom chambers (Ibidi GmbH) were purchased from Thistle Scientific Ltd
553 (Glasgow, UK).

554 **Dynamic Light Scattering**

555 The hydrodynamic diameter and colloidal stability of SiO₂ NPs was measured by dynamic
556 light scattering (DLS) using a Malvern Zetasizer Nano ZSP (Malvern Panalytical, Malvern, UK) at
557 a fixed 173° back-scattering angle. SiO₂ NPs were incubated in buffer (20 mM HEPES, 150 mM
558 NaCl, pH 7.4) for 1 hour and then measured three times to obtain the hydrodynamic diameter.
559 The same sample was measured again after 24 h and 48 h to evaluate the colloidal stability of
560 the NPs over time. The same instrument was used to measure the ζ potential of the SiO₂ NPs *via*
561 dynamic electrophoretic light scattering analysis (DELSA). In this case the scattering angle was
562 17° and the ζ potential was estimated from the measured electrophoretic mobility of the NPs using
563 the Smoluchowski approximation. DLS and DELSA results were processed using the Malvern
564 Zetasizer software.

565 DLS was also employed to determine the hydrodynamic size of DOPC LUVs before and
566 after incubation with SiO₂ NPs. The LUVs were diluted in buffer (20 mM HEPES, 150 mM NaCl,
567 pH 7.4) to a final lipid concentration of 100 μM. The LUVs suspension was incubated for 30
568 minutes with 30 μg/ml and 100 μg/ml of SiO₂ NPs, and a control sample without SiO₂ NPs was
569 used as control.

570 **Transmission electron microscopy**

571 Transmission electron microscopy (TEM) was conducted on an FEI Tecnai TF20 field
572 emission gun (FEG) TEM operating at 200 kV and fitted with a Gatan Orius SC600A CCD camera.
573 For TEM analysis, a drop of the dispersed sample was placed on a continuous carbon coated
574 copper grid (EM Resolutions, Sheffield, UK). After being left to dry, this was transferred to the
575 TEM. More than 1000 nanoparticles were analysed using Fiji to calculate the size distribution of
576 SiO₂ NPs.

577 **Preparation of large unilamellar vesicles**

578 Large unilamellar vesicles (LUVs) were prepared by the extrusion method. The desired
579 lipids were mixed at 25 mM in chloroform to get a final volume of 200 µl. The organic solvent was
580 evaporated under high vacuum overnight to get a dry lipid thin film which was then rehydrated
581 with 500 µl of buffer (20 mM HEPES, 150 mM NaCl, pH 7.4). The resulting suspension was
582 subjected to 10 freeze-thaw cycles and then extruded 11 times by passing through a 400 nm pore
583 size polycarbonate membrane (Whatman International Ltd., Maidstone, UK) using a LiposoFast
584 extruder (Avestin Inc.) to obtain a homogeneous population of LUVs.

585 **Lipid mixing assay**

586 The intervesicular lipid mixing was determined by measuring the Förster Resonance Energy
587 Transfer (FRET) between NBD and rhodamine (Rh). For these experiments, we prepared non-
588 labelled DOPC LUVs and DOPC LUVs labelled with 0.25 mol% NBD-DOPE and 0.25 mol% Rh-
589 DOPE. The two sets of LUVs were mixed in a 1:4 ratio (100 µM) and incubated during 30 minutes
590 with SiO₂ NPs at 3 µg/ml, 10 µg/ml, 30 µg/ml and 100 µg/ml. In addition, samples of LUVs non-
591 exposed to SiO₂ NPs (0 µg/ml) were used as negative control and samples of DOPC LUVs
592 labelled with 0.05 mol% NBD-DOPE and 0.05 mol% Rh-DOPE were used as full lipid mixing
593 control. The fluorescence intensity of the samples was measured between 500 nm and 650 nm

594 with a FluoroMax-Plus spectrofluorometer (Horiba Scientific), using the excitation wavelength of
595 NBD (460 nm). The maximum fluorescence intensity of NBD (I_{NBD} at 530 nm) and Rh (I_{Rh} at 590
596 nm) were used to calculate the FRET ratio (R) of each sample as $R = I_{Rh} / I_{NBD}$. The percentage
597 of lipid mixing was then calculated by normalising the FRET ratios of each sample (R_n) between
598 the baseline samples of LUVs untreated with SiO₂ NPs (R_0) and the full lipid mixing controls (R_{full}):

599
$$\% \text{ Lipid mixing} = \frac{R_n - R_0}{R_{full} - R_0} \times 100$$

600 Moreover, we also measured the maximum fluorescence intensity at 530 nm of DOPC LUVs
601 labelled only with 0.25 mol% NBD-DOPE. The values of the maximum fluorescence intensity of
602 NBD (donor) when the acceptor Rh is present (I_{DA}) and absent (I_D) was used to calculate the
603 FRET efficiency (E) using: $E = 1 - (I_{DA} / I_D)$.

604 **Electroformation of giant unilamellar vesicles**

605 Giant unilamellar vesicles (GUVs) were prepared by the electroformation method from 0.7
606 mM DOPC. Depending on the experiment, the GUVs were labelled with 0.5 mol% Rh-DOPE (Rh-
607 GUVs), 1 mol% DiO (DiO-GUVs), 1 mol% DiD or 0.5 mol% Laurdan, by adding the correspondent
608 dye to the DOPC solution in chloroform. For the electroformation, 15 μ L of lipid solution were
609 deposited on the conductive side of indium-tin oxide (ITO) coated glass slides and then dried
610 under a nitrogen stream to form a thin film. Then, the electroformation chamber was assembled
611 using two ITO slides, each in contact with a copper tape, separated by a 1.6 mm Teflon spacer.
612 The chamber was filled with 300 mM sucrose solution (300 mOsm/kg) and connected to a function
613 generator to apply an AC field. The frequency was set at 10 Hz and the voltage was gradually
614 increased from 1 V peak-to-peak (V_{pp}) to 5 V_{pp} over 15 minutes and maintained at 5 V_{pp} and 10
615 Hz for two hours. Finally, the frequency was gradually reduced to 0.1 Hz over 10 minutes to
616 facilitate the closure and detachment of GUVs from the slide. After electroformation, the GUVs
617 were diluted (1:5) with isotonic buffer (20 mM HEPES, 150 mM NaCl, pH 7.4, 300 mOsm/kg)

618 unless otherwise specified. For experiments where the membrane tension of the GUVs needs to
619 be osmotically modified, the osmolality of the buffer in which the GUVs were diluted after
620 electroformation was reduced or increased by 10 mOsm/kg to obtain tense GUVs or relaxed
621 GUVs, respectively.^{48, 62} The osmolality of the buffers was measured with a freezing point
622 depression Advanced Instruments 3320 osmometer.

623 To prepare GUVs loaded with fluorescent dextran, we added 1 mg/ml of TRITC-dextran 70
624 kDa to the sucrose solution used to rehydrate the lipid film in the electroformation chamber. The
625 electroformation was carried out as explained above. After the electroformation, unencapsulated
626 fluorescent dextran was removed from the medium by centrifugation washing protocol.⁶³ 200 μ l
627 of GUVs were diluted with 800 μ l of buffer (20 mM HEPES, 150 mM NaCl, pH 7.4) and then
628 centrifuged at 100x g for 3 minutes. The supernatant containing free dextran was removed and
629 the sedimented GUV are resuspended with 800 μ l of fresh buffer. The process was repeated 2
630 more times and in the final round the GUVs are resuspended to a final volume of 600 μ l.

631 **Confocal microscopy**

632 The GUV-fusion experiments were performed at room temperature on a Zeiss LSM-880
633 inverted laser scanning confocal microscope with a Plan-Apochromat 40x/1.4 Oil DIC M27
634 objective lens (NA = 1.4). The glass surfaces of the 8-well microscope chamber slides were
635 treated with 5% BSA solution in mili-Q water for 10 minutes and then rinsed with mili-Q water and
636 dried under a nitrogen stream to prevent GUVs from adhering and rupturing onto the glass. 200
637 μ l of GUVs were deposited into a well of the microscope slide and, once the GUVs were sunk in
638 the bottom of the well, 25 μ g/ml SiO₂ NPs were carefully added to the sample. All GUVs observed
639 in this study were between 8 μ m and 30 μ m (diameter of equatorial plane). DiO and Rh were
640 excited with a 488 nm argon laser and a 561 nm diode pumped solid state (DPSS) laser,
641 respectively. The emission of DiO was recorded between 493 nm and 553 nm and the emission
642 of Rh between 566 nm and 630 nm. The excitation and emission of TRITC dextran was the same

643 as for Rh. DiD was excited at 633 nm with a HeNe laser and its fluorescence emission was
644 detected between 640 nm and 750 nm.

645 **Laurdan spectral imaging**

646 GUVs labelled with 0.5 mol% Laurdan were prepared by electroformation. The spectral
647 imaging was acquired using the lambda mode of the Zeiss LSM880 confocal microscope. Laurdan
648 was excited at 405 nm and the fluorescence detection range was set between 410 nm and 550
649 nm with a spectral step of 8.9 nm per channel. Snapshots of Laurdan labelled GUVs were
650 acquired before and after exposure to 25 µg/ml SiO₂ NPs. If the lipid packing within the membrane
651 increases, the maximum fluorescence of Laurdan experience a blue shift from 490 nm (*I*₄₉₀) to
652 440 nm (*I*₄₄₀). The images were analysed with a Fiji plugin developed by Sezgin *et al*,⁶⁴ setting
653 440 nm and 490 nm as maximum emission wavelengths to calculate the GP values using the
654 following equation:

$$655 \quad GP = \frac{I_{440} - I_{490}}{I_{440} + I_{490}}$$

656 **Estimation of proportion of lipid mixed GUVs**

657 The proportion of GUVs undergoing fusion in the samples was quantified by taking confocal
658 microscopy tile scans of large sample areas containing a 1:1 (vol:vol) mixture of Rh-GUVs and
659 DiO-GUVs, after incubation with 25 µg/ml SiO₂ NPs for 30 minutes. GUVs with both dyes
660 colocalised in the membrane were counted as lipid mixed GUVs. The number of lipid mixed GUVs
661 in each tile image was counted manually and reported as the proportion respect the total number
662 of GUVs. These experiments were repeated for tense GUVs, neutral GUVs (in isotonic buffer)
663 and relaxed GUVs to assess the influence of the membrane tension in the fusion process.

664 **Detection of fusion intermediate states and estimation of lipid mixing rate**

665 A mixture of Rh-GUVs and DiO-GUVs (1:1; vol:vol) was exposed to 25 $\mu\text{g/ml}$ SiO_2 NPs.
666 Confocal microscopy time series were acquired to follow fusion processes taking place between
667 pairs of oppositely labelled GUVs over time. Images were analysed with Fiji to measure the
668 fluorescence intensity of each fluorophore in different regions of interest of the GUVs membranes.

669 For the estimation of the lipid mixing rate, we monitored the fluorescence increase over time
670 of one of the dyes when it invades the GUV initially labelled with the other fluorophore. For this
671 analysis, the fluorescence was normalised to the maximum intensity reached after fusion. The
672 data was fitted to an exponential function $f(x) = A(1-\exp(-t/\tau))$ where, A is the change in
673 fluorescence, t is the time passed since the lipids begin to mix and τ is the time constant. The rate
674 of lipid mixing is calculated as the diffusion coefficient (D): $D=\omega^2/4\tau$, where ω is the radius of a
675 circle with a surface area equivalent to the GUV analysed. The analysis of the images was
676 performed with Fiji and the data was fitted using Origin Pro.

677

678

679

680

681

682

683

684

685

686

687 **Supporting information**

688 TEM and DLS characterisation of SiO₂ NPs. Example of FRET spectrum and FRET ratio
689 and efficiency. Table of DLS data of individual LUVs samples. Influence of membrane tension in
690 fusion efficiency of LUVs measured by FRET. Ratio of volume change of GUVs after fusion through
691 different pathways. Confocal microscopy movies of GUV fusion.

692 **Data availability**

693 The datasets and movies that support the findings of this study are available in the White Rose
694 repository with the identifier (DOI tbc).

695 **ACKNOWLEDGEMENTS**

696 The authors thank Dr Nicole Hondow (School of Chemical and Process Engineering, University
697 of Leeds) for the acquisition of the TEM images of the nanoparticles. PAB acknowledges support
698 from a UK Engineering and Physical Sciences Research Council (EPSRC) grant
699 (EP/M027929/1). MAP is grateful to the University of Leeds for funding through the Lowson
700 Scholarship.

701

702

703 **REFERENCES**

- 704 1. Martens, S.; McMahon, H. T., Mechanisms of membrane fusion: disparate players and common
705 principles. *Nature Reviews Molecular Cell Biology* **2008**, 9 (7), 543-556.
- 706 2. Sudhof, T. C.; Rothman, J. E., Membrane Fusion: Grappling with SNARE and SM Proteins. *Science*
707 **2009**, 323 (5913), 474-477.
- 708 3. Gopfrich, K.; Platzman, I.; Spatz, J. P., Mastering Complexity: Towards Bottom-up Construction of
709 Multifunctional Eukaryotic Synthetic Cells. *Trends in Biotechnology* **2018**, 36 (9), 938-951.
- 710 4. Kretschmer, S.; Ganzinger, K. A.; Franquelim, H. G.; Schwille, P., Synthetic cell division via
711 membrane-transforming molecular assemblies. *Bmc Biology* **2019**, 17.

- 712 5. Walde, P.; Cosentino, K.; Engel, H.; Stano, P., Giant Vesicles: Preparations and Applications.
713 *Chembiochem* **2010**, *11* (7), 848-865.
- 714 6. Fenz, S. F.; Sengupta, K., Giant vesicles as cell models. *Integrative Biology* **2012**, *4* (9), 982-995.
- 715 7. Elani, Y.; Law, R. V.; Ces, O., Vesicle-based artificial cells as chemical microreactors with spatially
716 segregated reaction pathways. *Nature Communications* **2014**, *5*.
- 717 8. Hindley, J. W.; Elani, Y.; McGilvery, C. M.; Ali, S.; Bevan, C. L.; Law, R. V.; Ces, O., Light-triggered
718 enzymatic reactions in nested vesicle reactors. *Nature Communications* **2018**, *9*.
- 719 9. Blanken, D.; Foschepoth, D.; Serrao, A. C.; Danelon, C., Genetically controlled membrane
720 synthesis in liposomes. *Nature communications* **2020**, *11* (1), 4317-4317.
- 721 10. Berhanu, S.; Ueda, T.; Kuruma, Y., Artificial photosynthetic cell producing energy for protein
722 synthesis. *Nature Communications* **2019**, *10*.
- 723 11. Schwille, P.; Spatz, J.; Landfester, K.; Bodenschatz, E.; Herminghaus, S.; Sourjik, V.; Erb, T. J.;
724 Bastiaens, P.; Lipowsky, R.; Hyman, A.; Dabrock, P.; Baret, J. C.; Vidakovic-Koch, T.; Bieling, P.; Dimova,
725 R.; Mutschler, H.; Robinson, T.; Tang, T. Y. D.; Wegner, S.; Sundmacher, K., MaxSynBio: Avenues
726 Towards Creating Cells from the Bottom Up. *Angewandte Chemie-International Edition* **2018**, *57* (41),
727 13382-13392.
- 728 12. Ganzinger, K. A.; Schwille, P., More from less - bottom-up reconstitution of cell biology. *Journal of*
729 *Cell Science* **2019**, *132* (4).
- 730 13. Tsugane, M.; Suzuki, H., Reverse Transcription Polymerase Chain Reaction in Giant Unilamellar
731 Vesicles. *Scientific Reports* **2018**, *8*.
- 732 14. Jahn, R.; Lang, T.; Sudhof, T. C., Membrane fusion. *Cell* **2003**, *112* (4), 519-533.
- 733 15. Chernomordik, L. V.; Zimmerberg, J.; Kozlov, M. M., Membranes of the world unite! *Journal of Cell*
734 *Biology* **2006**, *175* (2), 201-207.
- 735 16. Lei, G. H.; MacDonald, R. C., Lipid bilayer vesicle fusion: Intermediates captured by high-speed
736 microfluorescence spectroscopy. *Biophysical Journal* **2003**, *85* (3), 1585-1599.
- 737 17. Lira, R. B.; Robinson, T.; Dimova, R.; Riske, K. A., Highly Efficient Protein-free Membrane Fusion:
738 A Giant Vesicle Study. *Biophysical Journal* **2019**, *116* (1), 79-91.
- 739 18. Löffler, P. M. G.; Ries, O.; Rabe, A.; Okholm, A. H.; Thomsen, R. P.; Kjems, J.; Vogel, S., A DNA-
740 Programmed Liposome Fusion Cascade. *Angewandte Chemie-International Edition* **2017**, *56* (43), 13228-
741 13231.
- 742 19. Nikolaus, J.; Stockl, M.; Langosch, D.; Volkmer, R.; Herrmann, A., Direct Visualization of Large and
743 Protein-Free Hemifusion Diaphragms. *Biophysical Journal* **2010**, *98* (7), 1192-1199.
- 744 20. Mora, N. L.; Boyle, A. L.; Kolck, B. J. v.; Rossen, A.; Pokorna, S.; Koukalova, A.; Sachl, R.; Hof,
745 M.; Kros, A., Controlled Peptide-Mediated Vesicle Fusion Assessed by Simultaneous Dual-Colour Time-
746 Lapsed Fluorescence Microscopy. *Scientific reports* **2020**, *10* (1), 3087-3087.
- 747 21. Mondal Roy, S.; Sarkar, M., Membrane fusion induced by small molecules and ions. *Journal of*
748 *lipids* **2011**, *2011*, 528784-528784.
- 749 22. Bolognesi, G.; Friddin, M. S.; Salehi-Reyhani, A.; Barlow, N. E.; Brooks, N. J.; Ces, O.; Elani, Y.,
750 Sculpting and fusing biomimetic vesicle networks using optical tweezers. *Nature Communications* **2018**, *9*.
- 751 23. Vivek, A.; Bolognesi, G.; Elani, Y., Fusing Artificial Cell Compartments and Lipid Domains Using
752 Optical Traps: A Tool to Modulate Membrane Composition and Phase Behaviour. *Micromachines* **2020**, *11*
753 (4).
- 754 24. Haluska, C. K.; Riske, K. A.; Marchi-Artzner, V.; Lehn, J. M.; Lipowsky, R.; Dimova, R., Time scales
755 of membrane fusion revealed by direct imaging of vesicle fusion with high temporal resolution. *Proceedings*
756 *of the National Academy of Sciences of the United States of America* **2006**, *103* (43), 15841-15846.

- 757 25. Rorvig-Lund, A.; Bahadori, A.; Semsey, S.; Bendix, P. M.; Oddershede, L. B., Vesicle Fusion
758 Triggered by Optically Heated Gold Nanoparticles. *Nano Letters* **2015**, *15* (6), 4183-4188.
- 759 26. Werner, M.; Auth, T.; Beales, P. A.; Fleury, J. B.; Hook, F.; Kress, H.; Van Lehn, R. C.; Muller, M.;
760 Petrov, E. P.; Sarkisov, L.; Sommer, J. U.; Baulin, V. A., Nanomaterial interactions with biomembranes:
761 Bridging the gap between soft matter models and biological context. *Biointerphases* **2018**, *13* (2), 028501.
- 762 27. Vutukuri, H. R.; Hoore, M.; Abaurrea-Velasco, C.; van Buren, L.; Dutto, A.; Auth, T.; Fedosov, D.
763 A.; Gompper, G.; Vermant, J., Active particles induce large shape deformations in giant lipid vesicles.
764 *Nature* **2020**, *586* (7827), 52-+.
- 765 28. Contini, C.; Hindley, J. W.; Macdonald, T. J.; Barritt, J. D.; Ces, O.; Quirke, N., Size dependency of
766 gold nanoparticles interacting with model membranes. *Communications Chemistry* **2020**, *3* (1).
- 767 29. Zuraw-Weston, S.; Wood, D. A.; Torres, I. K.; Lee, Y.; Wang, L. S.; Jiang, Z. W.; Lazaro, G. R.;
768 Wang, S. Y.; Rodal, A. A.; Hagan, M. F.; Rotello, V. M.; Dinsmore, A. D., Nanoparticles binding to lipid
769 membranes: from vesicle-based gels to vesicle tubulation and destruction. *Nanoscale* **2019**, *11* (39), 18464-
770 18474.
- 771 30. Tahir, M. A.; Guven, Z. P.; Arriaga, L. R.; Tinao, B.; Yang, Y. S. S.; Bekdemir, A.; Martin, J. T.;
772 Bhanji, A. N.; Irvine, D.; Stellacci, F.; Alexander-Katz, A., Calcium-triggered fusion of lipid membranes is
773 enabled by amphiphilic nanoparticles. *Proceedings of the National Academy of Sciences of the United*
774 *States of America* **2020**, *117* (31), 18470-18476.
- 775 31. Zhang, S. W.; Nelson, A.; Beales, P. A., Freezing or Wrapping: The Role of Particle Size in the
776 Mechanism of Nanoparticle-Biomembrane Interaction. *Langmuir* **2012**, *28* (35), 12831-12837.
- 777 32. Alkhamash, H. I.; Li, N.; Berthier, R.; de Planque, M. R. R., Native silica nanoparticles are
778 powerful membrane disruptors. *Physical Chemistry Chemical Physics* **2015**, *17* (24), 15547-15560.
- 779 33. Wei, X. R.; Jiang, W.; Yu, J. C.; Ding, L.; Hu, J. T.; Jiang, G. B., Effects of SiO₂ nanoparticles on
780 phospholipid membrane integrity and fluidity. *Journal of Hazardous Materials* **2015**, *287*, 217-224.
- 781 34. Struck, D. K.; Hoekstra, D.; Pagano, R. E., Use of resonance energy-transfer to monitor membrane-
782 fusion. *Biochemistry* **1981**, *20* (14), 4093-4099.
- 783 35. Ibarguren, M.; Bomans, P. H. H.; Ruiz-Mirazo, K.; Frederik, P. M.; Alonso, A.; Goni, F. M.,
784 Thermally-induced aggregation and fusion of protein-free lipid vesicles. *Colloids and Surfaces B-
785 Biointerphases* **2015**, *136*, 545-552.
- 786 36. Nazemidashtarjandi, S.; Farnoud, A. M., Membrane outer leaflet is the primary regulator of
787 membrane damage induced by silica nanoparticles in vesicles and erythrocytes. *Environmental Science-
788 Nano* **2019**, *6* (4), 1219-1232.
- 789 37. Akimov, S. A.; Molotkovsky, R. J.; Kuzmin, P. I.; Galimzyanov, T. R.; Batishchev, O. V., Continuum
790 Models of Membrane Fusion: Evolution of the Theory. *International journal of molecular sciences* **2020**, *21*
791 (11).
- 792 38. Meher, G.; Chakraborty, H., Membrane Composition Modulates Fusion by Altering Membrane
793 Properties and Fusion Peptide Structure. *Journal of Membrane Biology* **2019**, *252* (4-5), 261-272.
- 794 39. Wei, X. R.; Yu, J. C.; Ding, L.; Hu, J. T.; Jiang, W., Effect of oxide nanoparticles on the morphology
795 and fluidity of phospholipid membranes and the role of hydrogen bonds. *Journal of Environmental Sciences*
796 **2017**, *57*, 221-230.
- 797 40. Kozlovsky, Y.; Chernomordik, L. V.; Kozlov, M. M., Lipid intermediates in membrane fusion:
798 Formation, structure, and decay of hemifusion diaphragm. *Biophysical Journal* **2002**, *83* (5), 2634-2651.
- 799 41. Kozlov, M. M.; Chernomordik, L. V., Membrane tension and membrane fusion. *Current Opinion in*
800 *Structural Biology* **2015**, *33*, 61-67.
- 801 42. Shillcock, J. C.; Lipowsky, R., Tension-induced fusion of bilayer membranes and vesicles. *Nature*
802 *Materials* **2005**, *4* (3), 225-228.

- 803 43. Liu, X. J.; Tian, F. L.; Yue, T. T.; Zhang, X. R.; Zhong, C. L., Pulling force and surface tension drive
804 membrane fusion. *Journal of Chemical Physics* **2017**, *147* (19).
- 805 44. Kliesch, T. T.; Dietz, J.; Turco, L.; Halder, P.; Polo, E.; Tarantola, M.; Jahn, R.; Janshoff, A.,
806 Membrane tension increases fusion efficiency of model membranes in the presence of SNAREs. *Scientific*
807 *Reports* **2017**, *7*.
- 808 45. Lu, T.; Guo, H. X., How the Membranes Fuse: From Spontaneous to Induced. *Advanced Theory*
809 *and Simulations* **2019**, *2* (7), 10.
- 810 46. Kozlovsky, Y.; Kozlov, M. M., Stalk model of membrane fusion: Solution of energy crisis.
811 *Biophysical Journal* **2002**, *82* (2), 882-895.
- 812 47. Heo, P.; Park, J. B.; Shin, Y. K.; Kweon, D. H., Visualization of SNARE-Mediated Hemifusion
813 between Giant Unilamellar Vesicles Arrested by Myricetin. *Frontiers in Molecular Neuroscience* **2017**, *10*.
- 814 48. Arribas Perez, M.; Moriones, O. H.; Bastus, N. G.; Puentes, V.; Nelson, A.; Beales, P. A.,
815 Mechanomodulation of Lipid Membranes by Weakly Aggregating Silver Nanoparticles. *Biochemistry* **2019**,
816 *58* (47), 4761-4773.
- 817 49. Akimov, S. A.; Volynsky, P. E.; Galimzyanov, T. R.; Kuzmin, P. I.; Pavlov, K. V.; Batishchev, O. V.,
818 Pore formation in lipid membrane II: Energy landscape under external stress. *Scientific Reports* **2017**, *7*
819 (1), 12509.
- 820 50. D'Agostino, M.; Risselada, H. J.; Endter, L. J.; Comte-Miserez, V.; Mayer, A., SNARE-mediated
821 membrane fusion arrests at pore expansion to regulate the volume of an organelle. *Embo Journal* **2018**, *37*
822 (19).
- 823 51. Coomer, C. A.; Carlon-Andres, I.; Iliopoulou, M.; Dustin, M. L.; Compeer, E. B.; Compton, A. A.;
824 Padilla-Parra, S., Single-cell glycolytic activity regulates membrane tension and HIV-1 fusion. *Plos*
825 *Pathogens* **2020**, *16* (2).
- 826 52. Bassereau, P.; Jin, R.; Baumgart, T.; Deserno, M.; Dimova, R.; Frolov, V. A.; Bashkirov, P. V.;
827 Grubmuller, H.; Jahn, R.; Risselada, H. J.; Johannes, L.; Kozlov, M. M.; Lipowsky, R.; Pucadyil, T. J.; Zeno,
828 W. F.; Stachowiak, J. C.; Stamou, D.; Breuer, A.; Lauritsen, L.; Simon, C.; Sykes, C.; Voth, G. A.; Weikl, T.
829 R., The 2018 biomembrane curvature and remodeling roadmap. *Journal of Physics D-Applied Physics*
830 **2018**, *51* (34).
- 831 53. Risselada, H. J.; Smirnova, Y.; Grubmuller, H., Free Energy Landscape of Rim-Pore Expansion in
832 Membrane Fusion. *Biophysical Journal* **2014**, *107* (10), 2287-2295.
- 833 54. Cevc, G.; Richardsen, H., Lipid vesicles and membrane fusion. *Advanced Drug Delivery Reviews*
834 **1999**, *38* (3), 207-232.
- 835 55. Tanaka, T.; Yamazaki, M., Membrane fusion of giant unilamellar vesicles of neutral phospholipid
836 membranes induced by La³⁺. *Langmuir* **2004**, *20* (13), 5160-5164.
- 837 56. Wang, L.; Seeley, E. S.; Wickner, W.; Merz, A. J., Vacuole fusion at a ring of vertex docking sites
838 leaves membrane fragments within the organelle. *Cell* **2002**, *108* (3), 357-369.
- 839 57. Mattie, S.; McNally, E. K.; Karim, M. A.; Vali, H.; Brett, C. L., How and why intraluminal membrane
840 fragments form during vacuolar lysosome fusion. *Molecular Biology of the Cell* **2017**, *28* (2), 309-321.
- 841 58. Raphael, R. M.; Waugh, R. E., Accelerated interleaflet transport of phosphatidylcholine molecules
842 in membranes under deformation. *Biophysical Journal* **1996**, *71* (3), 1374-1388.
- 843 59. Doktorova, M.; Heberle, F. A.; Marquardt, D.; Rusinova, R.; Sanford, R. L.; Peyear, T. A.; Katsaras,
844 J.; Feigenson, G. W.; Weinstein, H.; Andersen, O. S., Gramicidin Increases Lipid Flip-Flop in Symmetric
845 and Asymmetric Lipid Vesicles. *Biophysical Journal* **2019**, *116* (5), 860-873.
- 846 60. Gardner, J. M.; Abrams, C. F., Lipid flip-flop vs. lateral diffusion in the relaxation of hemifusion
847 diaphragms. *Biochimica Et Biophysica Acta-Biomembranes* **2018**, *1860* (7), 1452-1459.

- 848 61. Strobl, F. G.; Seitz, F.; Westerhausen, C.; Reller, A.; Torrano, A. A.; Brauchle, C.; Wixforth, A.;
849 Schneider, M. F., Intake of silica nanoparticles by giant lipid vesicles: influence of particle size and
850 thermodynamic membrane state. *Beilstein Journal of Nanotechnology* **2014**, *5*, 2468-2478.
- 851 62. Booth, A.; Marklew, C. J.; Ciani, B.; Beales, P. A., In Vitro Membrane Remodeling by ESCRT is
852 Regulated by Negative Feedback from Membrane Tension. *iScience* **2019**, *15*, 173-184.
- 853 63. Imam, Z. I.; Kenyon, L. E.; Ashby, G.; Nagib, F.; Mendicino, M.; Zhao, C.; Gadok, A. K.; Stachowiak,
854 J. C., Phase-Separated Liposomes Enhance the Efficiency of Macromolecular Delivery to the Cellular
855 Cytoplasm. *Cellular and Molecular Bioengineering* **2017**, *10* (5), 387-403.
- 856 64. Sezgin, E.; Waithe, D.; de la Serna, J. B.; Eggeling, C., Spectral Imaging to Measure Heterogeneity
857 in Membrane Lipid Packing. *Chemphyschem* **2015**, *16* (7), 1387-1394.

858

859

860

861

862